



Doping of few-layered graphene and carbon nanotubes using ion implantation

U. Bangert,^{1,*} A. Bleloch,² M. H. Gass,² A. Seepujak,¹ and J. van den Berg³

¹*School of Materials Science, University of Manchester, Grosvenor Street, Manchester M1 7HS, United Kingdom*

²*School of Engineering, University of Liverpool, Liverpool L69 3BX, United Kingdom*

³*School of Computing, Science and Engineering, University of Salford, Salford, Greater Manchester M5 4WT, United Kingdom*

(Received 11 November 2009; revised manuscript received 17 April 2010; published 18 June 2010)

Doping of nanostructured materials using a clean, efficient, and site-selective route such as ion implantation would be hugely desirable for realization of large-scale production methods. Here, ion implantation is used to create uniform impurity-atom densities which are both dose and spatially controlled within multiwalled carbon nanotubes and graphene. The technique is demonstrated for a range of dopants, including silver, representing a likely candidate for optical enhancement, and boron, which is predicted to introduce a plasmon within the visible-frequency regime. Electron energy-loss spectroscopy performed within an aberration-corrected scanning transmission electron microscope, in combination with high-angle-annular-dark-field imaging, is used to pinpoint and identify the bonding configuration of single foreign species within the matrix.

DOI: [10.1103/PhysRevB.81.245423](https://doi.org/10.1103/PhysRevB.81.245423)

PACS number(s): 68.37.Ma, 61.48.De

Doping of a matrix beyond the solid solubility limit¹ via ion implantation represents a process critical in all semiconductor devices and has become a standard large-scale industrial technology; if as a consequence of the ongoing down scaling of components next-generation nanoelectronic materials, carbon nanotubes (CNTs) and graphene, will be employed on a commercial scale, they will have to be tailored by processes paralleling those of silicon technology, including use of ion-beam methods.

CNT—and more recently graphene—transistors have been demonstrated, and exotic CNT transistors employing spin-polarized transport (with ultimate goal to achieve the quantum computer) are not far from reality. CNTs are moreover excellent contenders for nanoconnectors, waveguides, light emitters,² and solar-cell materials, and here their full potential is only realized when their surface plasmons (originating from the delocalized π -electron system) can be tailored to exhibit optical energies and can furthermore couple with optical electromagnetic fields. Graphene has furthermore been suggested for sensor applications due to the sensitivity of its electronic structure to adsorbates.³ If nanocarbons are to enter the realms of practical devices, then reliable and controlled doping has to be mastered in all cases.

Doping of carbon nanotubes at levels which influence their electronic properties, through to levels at which material modification is induced (to achieve superhard phases/composites, hydrogen storage, or encapsulated nanoconductors), is a most important aspect in nanotube research and development to date. Doping has been achieved via a variety of methods; these encompass routes of little flexibility, with next to no control of the product, to routes with some degree of control for product engineering, culminating in modulation doping to achieve the single-walled CNT transistor.⁴ Methods commonly used are substitution reactions during CNT growth, e.g., in arc discharge methods (mostly for B and N, where the dopant elements are added in solid or vapor form compounds), and also in laser ablation of graphite, or in postgrowth redox reactions, or thermochemical, electrochemical, and biochemical processes (adding functionalized groups), and physisorption/chemical adsorption.^{5–10}

A major effort has gone into doping of single-walled

CNTs. These can be doped, or intercalated, with electron donors or acceptors via vapor, liquid phase, or electrochemistry, resulting in enhanced electrical conductivity, conduction-electron paramagnetism and partial or complete reversibility. Structural information is sketchy at best, but it is clear that the quality of produced materials is limited (partly due to and solvent-related effects). Attempts to change the electronic structure of graphene have consisted of “dosing” with foreign materials (e.g., hydrogen), but this again is a process of little control. It appears that ion implantation, which has long been known to be a clean, efficient, and site-selective doping process in semiconductor technology, is the logical step forward for doping of nanocarbons.

Turning to the dopant elements themselves: well-researched dopants are N and B,^{11–14} which are said to take substitutional places at low concentrations. Boron enhances metallicity and crystallinity and can result in ordered structures, whereas N induces buckling and cross linking resulting in significant sp^3 fractions and increased hardness. There are impressive reports of the evolution of morphology of single-walled CNTs with increasing B doping,¹⁴ from defect introduction at low B levels to graphitization and nanoparticle formation at high levels. In the literature, B has not been found to go substitutionally into the graphite lattice or to constitute a low-dose uniform dopant; it was found to form phases with other elements, e.g., N, within the graphite. The opposite is true for N, here the predicted superhard phases could not be achieved, but nanoscale investigations of N incorporation suggest homogeneous low-level incorporation into the CNT wall, e.g., Ref. 15.

Other much investigated elements are alkali metals. Doping here often results in intercalation in the intershell spaces in multiple-walled CNTs and inside or between single-walled CNTs and “mats” thereof, respectively. The reaction of intercalation can be carried out in the vapor or liquid phase and electrochemically.^{16,17} Studies of structural and electronic properties have been carried out by a battery of complementary techniques, and inhomogeneous doping models have been suggested.¹⁸ The conductivity generally increases by alkali doping, e.g., Ref. 19, and detailed charge-transfer models between the alkali and C in single-walled CNTs have

been deduced experimentally²⁰ and theoretically.²¹ Alkali elements are known to induce Drude plasmons at $\sim 1\text{--}2.5$ eV, depending on the element and concentration.²² From both a geometrical and microstructural point of view, CNTs would represent ideal waveguides; if propagating plasmon modes could be created this would enable fabrication of CNTs nanowaveguides of considerable length. Plasmons have radiative and nonradiative modes. Nonradiative modes can be transformed into radiative ones; thus coupling with an electromagnetic field would result in a waveguiding light emitter or absorber. Silver is known to exhibit very strong radiative plasmons.²³ Silver has already been exploited as “antennae” and light concentrators;²⁴ intercalation of CNTs with silver can be expected to produce efficient nanotube light guides and emitters also.

In all doping scenarios performed using ion implantation, it is critical to know: (i) whether dopants actually assume a configuration within the crystal lattice; (ii) the location and distribution of dopants; (iii) which bonding configuration dopants adopt in the host; and (iv) to what extent the electronic and structural environment is modified by the presence of the dopant.

Aberration-corrected transmission electron microscopy (TEM) enables the pinpointing of single-impurity atoms in a matrix. If the element is heavier than the matrix, it can be detected directly via high-angle-annular-dark-field (HAADF) imaging in a scanning transmission electron microscope (STEM). HAADF images are recorded with electrons having undergone incoherent elastic scattering at high angles; the intensity of the HAADF image is approximately proportional to $Z^{1.7}$ of the atoms illuminated by the probe. If the element is of the same or lower Z number, direct HAADF imaging will not usually reveal it. However, by employing electron energy-loss spectroscopy (EELS) and making use of the high spatial resolution of, e.g., an aberration-corrected STEM, positions of single light atoms can be detected by their EEL signals and be correlated with atomic positions in simultaneously obtained lattice resolution HAADF and bright-field (BF) images. Since inelastic scattering cross-sections are on the order of 1 nm^2 , impurity atoms of greater density than 1 atom per square nanometer would not, via EELS, be detected as single atoms. To detect single-impurity atoms at all, their signal has to be maximized against the signal of the matrix. This can be achieved by using the smallest possible electron probe ($\sim 1\text{ Å}$ in diameter) and a very thin sample; in this case individual atomic columns can be illuminated which would contain few atoms altogether with solely one of them being the impurity atom. This represents the situation applicable to dopants in few-layered CNTs or graphene. If the sample contains disperse impurities, an angstrom-sized e-probe scanned with step size 1 nm should reveal these: an impurity density of 1 nm^{-2} corresponds to a signal in each pixel; to achieve the same number of signal pixels with an order of magnitude lower impurity density would require an order of magnitude larger scan area. Small (nm) scan step sizes s with seconds of acquisition time per scan point can corrupt the sample, less frequent sampling in larger step-sized scans (using the same probe size for optimum signal/matrix ratio) may be less invasive, however, in order to obtain the same number of signal pixels the scan area would have to be scaled with s^2 .

Ion implantation was used to create controlled impurity densities of uniform distribution in nanotubes and graphene. However, before endeavoring on the aim of the present investigation, namely, to establish points (i)–(iv) above, we briefly discuss the structural impact of low-energy ion bombardment. Studies of fullerenes irradiated with heavy ions, over the past decade, state varying effects, from damage to chemical doping²⁵ to ferromagnetic ordering.²⁶ Krashennnikov and Banhart²⁷ gave a comprehensive review on engineering of nanocarbons with electrons and ion beams, concluding that “irradiation of nanostructures does not necessarily destroy them, but may result in many fascinating phenomena that can be readily used for engineering nanosystems and tailoring their properties.” They also review the most prolific defects on irradiation to be vacancy constellations, which undergo reconstruction, as “curved graphitic structures have self-healing tendencies.” In this paper we try to establish the “fate” of implanted ions, i.e., how they are incorporated and which structural environment they reside in; we also carry out a preliminary exploration of a possible electronic functionalization.

It has previously been estimated that at an energy of 200 eV, ions of Z ranging from carbon to xenon are stopped within the first three graphene layers with little loss of structural integrity.²⁸ The probability for stopping ions is greatest when the traversed sample thickness is largest. Nanotubes implanted perpendicularly to their axis present such locations where the basal planes are almost parallel to the ion trajectories; when the planes are exactly parallel, however, ions may undergo channeling, resulting in less efficient stopping; implants may also not be stopped by very few layers, when the coincidence is perpendicular to the sheets.

Regarding the issue of damage, we have compared the structure of pristine with ion-implanted tubes in high-resolution TEM with as little e-beam exposure as possible. Figures 1(a)–1(c) show representative images of few-walled and multiple-walled nanotubes for all scenarios. The tubes in *all* samples (implanted and unimplanted) exhibit different types of perfection, and the ratio of crumpled tubes and tubes with partial corruption of the outermost wall to straight ones with largely intact outermost walls is similar in all samples. The images shown in Fig. 1 for the implanted tubes are for the highest received doses ($2 \times 10^{15}\text{ cm}^{-2}$; see Table I). Even in this case the differences to pristine tubes are not obvious. If anything, damage effects due to the e beam are dominant in all the samples. We suspect that the “wavy” appearance of the thinnest tubes in images (a)–(c) arises from e-beam exposure in the 300 keV Tecnai, albeit only for the time of focusing and image acquisition. Figures 1(d) and 1(e) are taken in an aberration-corrected TEM (Titan; 300 keV) and compare Ag-implanted tubes at first image taking and at image taking following prolonged exposure to the electron beam. The ion-implanted tubes show high structural integrity, but the three-walled tube has started to crumple during e-beam exposure. Generally it was observed that few-walled tubes loose structural integrity more rapidly and markedly than those with many walls. Examples of tubes having received the smaller ion dose of 10^{14} cm^{-2} can be seen in Figs. 3 and 4. Again there is no evidence of structural damage, e.g., disruption of graphene sheets, amorphization, etc., when compared to unimplanted tubes.

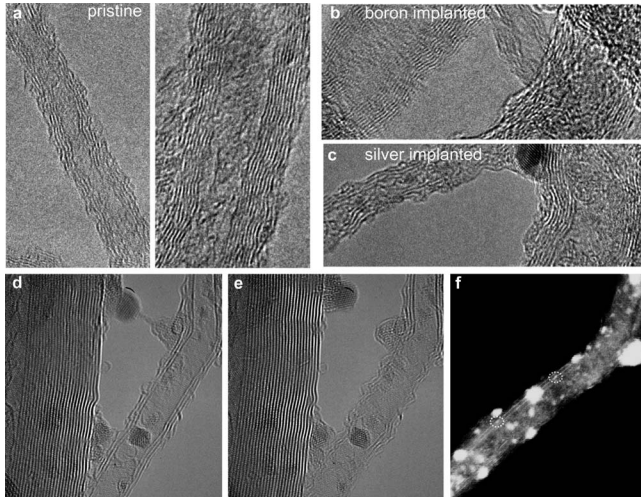


FIG. 1. [(a)–(c)] HREM images obtained in a Tecnai F30 for direct comparison of pristine few- and multiwalled carbon nanotubes (a) and B- and Ag-doped tubes, (b) and (c), respectively, the latter both ion implanted to a dose of $2 \times 10^{15} \text{ cm}^{-2}$ at 200 eV. The structural integrity does not appear higher in the pristine tubes. [(d) and (e)] HREM images obtained in a Titan 80–300 of the same Ag-implanted tubes as in (c) at superior resolution to show details of the Ag clusters and also the effect of e-beam irradiation at prolonged time on small tubes. (f) HAADF image obtained in a Titan of a three-walled tube, showing Ag-atom aggregates from nanometer-sized clusters clinging to the tube exterior, to subnanometer clusters which have partially formed inside the tube, to intercalated single atoms (dashed circles).

We have implanted cobalt, silver, nitrogen, and boron into CNTs and also endeavored on implanting boron into single- and few-layered graphene. Ion implantation was carried out in the Salford University low-energy implanter; implantation details for CNTs and graphene are given in Table I. To provide a reasonable degree of stopping efficiency and ion density, nitrogen, boron, and cobalt were implanted into CNTs at 100 eV and 10^{14} cm^{-2} , and boron into graphene, at 100 eV and 10^{14} cm^{-2} . The implantation energy of 200 eV for silver was chosen so as to yield a similar implantation depth as that of cobalt. A higher dose of $2 \times 10^{15} \text{ cm}^{-2}$ (in the last two examples of B and Ag) was employed to significantly change electron densities (see later explanations). Cobalt and silver are metals, which can be expected to intercalate, and whose presence and location, owing to their high-Z number, can be directly ascertained from HAADF imaging.

Ion implantation was carried out into TEM-ready

TABLE I. Implantation parameters for various dopants.

Species	Energy (eV)	Dose $\times 10^{14} (\text{cm}^{-2})$
Boron (CNT and graphene)	100	1
Nitrogen (CNT)	100	1
Cobalt (CNT)	100	1
Silver (CNT)	200	20
Boron (CNT)	200	20

samples: commercially available CNTs were dispersed by sonication in distilled water and the solution dripped onto lacey carbon-film-coated TEM copper-mesh grids. All glass-ware were vigorously washed in ethanol in order to prevent silicon contamination. The CNTs were of high purity and graphiticity and possessed few (<10) walls. Graphene samples were obtained by micromechanical cleaving and exfoliation from highly oriented pyrolytic (HOP) graphite. The procedure has been widely published and is explained in greater detail, e.g., Ref. 29.

High-resolution images in Fig. 2(f) were obtained in HAADF and BF mode in a dedicated cold-field emission STEM (Daresbury SuperSTEM with C_s corrector³⁰), operated at 80 kV, using a probe size of $\sim 1 \text{ \AA}$ and a probe current of $\sim 100 \text{ pA}$. Electron energy-loss data were acquired in spectrum imaging (SI) mode³¹ with an Enfina EEL spectrometer and 1 s acquisition time per spectrum. The theoretical value for knock-on damage is 120 keV, although a value of $\sim 100 \text{ keV}$ is nearer to observations. Close comparison of the microstructure before and after EEL measurements guided us to exclude radiation effects in the present data. The plasmon images in the last part of the paper were obtained at 100 keV in the NorthWest STEM equipped with an Enfina EEL spectrometer providing an energy resolution of 0.3 eV, which, owing to availability of high-energy dispersions, is optimized for low-loss EELS.

Silver nanoparticles are famously known for their optical behavior owing to strong surface plasmons resonances³² in the uv-visible spectrum. The high-implantation dose for silver ions was chosen in order to investigate whether Ag incorporated into CNTs can make the CNT optically active by inducing a plasmon at optical energies inside the CNT wall; we expect that high-intercalation levels would have to be achieved to induce such a plasmon. Boron is predicted to introduce a valence band, i.e., “intrapband” plasmon, which would also have its resonance in the visible/near-uv regime; for this reason boron, too, was implanted into CNTs at the higher dose of $2 \times 10^{15} \text{ cm}^{-2}$ at 200 eV.

Cobalt-implanted CNTs are detailed in Fig. 2. The implantation density of 1 atom per square nanometer in the case of cobalt ions is not reflected in HAADF images [Fig. 2(b)]. Bright spots (representing Co ions) are sparse, and it appears that less than 10% of the Co is retained in the tube. Of this fraction, a considerable amount may be integrated into surface contamination, which is omnipresent. Furthermore, the two-dimensional (2D) projection makes it difficult to decide whether impurity atoms are inside or on top of objects. However, time-series HAADF images, in which the same area is repeatedly scanned, either as function of time alone (all other parameters kept the same) or as function of focus and time, reveal small displacements of impurity atoms due to interaction with the e beam in subsequent scan images. Such displacements occur if atoms are not integrated or covalently bonded, as would be the case for intercalated impurities. Looking at the central regions of the CNT projections, we cannot tell whether Co atoms move between graphene sheets or on the tube surface. However, in regions with vertical CNT-wall projections, if atom trajectories are observed to have components vertical to the walls, these atoms most likely migrate on the CNT surface. Trajectories strictly par-

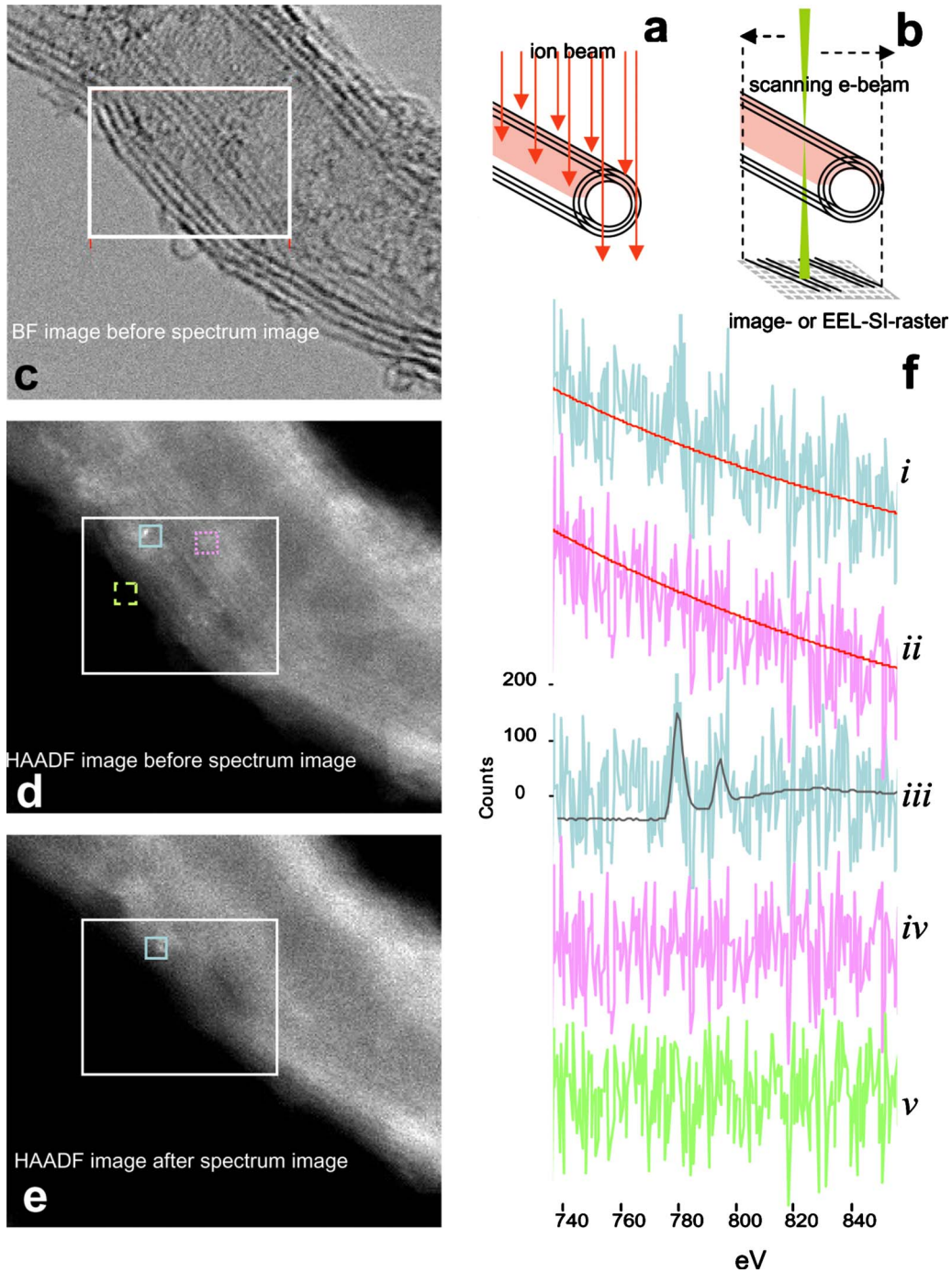


FIG. 2. (Color online) (a) Schematics of CNT ion implantation and (b) of STEM and EEL spectrum imaging. [(c) and (d)] SuperSTEM high-resolution BF and HAADF image of a multiple-walled CNT implanted with Co at 100 eV and 10^{14} ions cm^{-2} . The region where an SI was taken is framed in white. The small solid frame (pale blue) contains a Co atom on the surface. (e) HAADF image after the SI acquisition. The Co atom is still within the same frame. (f) Top to bottom: raw EEL spectrum from the small, solid-line frame in (d) and (e) with overlaid background fit showing the Co-*L* edge signal (i), raw spectrum from the dotted small frame without Co atom (pink) in (d) with overlaid background fit (ii), background-subtracted spectrum from the solid-line small frame with overlaid Co *L*-edge standard spectrum (iii), background-subtracted spectrum from the dotted frame in (d) (iv), spectrum from the dashed small frame (green) in (d) showing vacuum counts (v).

allel to the walls (in fact, in between walls) on the other hand suggest intercalated atoms, which move between graphene sheets. The small, light (blue online), solid-line frame in Figs. 2(d) and 2(e) contains a cobalt atom as evidenced by the white dot in the HAADF image as well as by the cobalt

L-edge EEL signal in the uppermost spectrum (i) in Fig. 2(f) (raw data with background fit overlaid), taken from the named, $0.34 \times 0.34 \text{ nm}^2$ pixel of the corresponding SI,³¹ which was acquired over the large white-framed area. Although the HAADF focus has slightly changed the Co atom

can be seen in the same pixel in Fig. 2(e) after the SI was taken. Such Co signals were obtained in very few positions, and they were, as in this case, of surface atoms, as these can be most easily focused on. From time-series HAADF imaging, we deduce that less than 50% of the detected Co atoms are in positions between CNT walls. Hence overall less than 5% of the implanted Co ions appear to be retained intercalated in the CNT walls. The second spectrum (ii) down in Fig. 2(f) shows raw data from the pixel framed by a dotted line [pink online; Fig. 2(d)] without a Co atom. The third and the fourth curves [(iii) and (iv)] down are background-subtracted spectra with and without the Co atom; a standard Co *L*-edge spectrum (dark gray curve) is overlaid on spectrum (iii). The bottom curve (v) is from the dashed-framed pixel (light green online) in Fig. 2(d) and shows the noise level of vacuum.

In an aberration- (probe-) corrected microscope, the focal point can be controlled with a precision of 1 nm, and where atoms are sitting within the tube can be judged by the way they go in and out of focus when the latter is changed in steps from the entrance to the exit surface in a through-focus series. To substantiate the results of retention for intercalation with metals (but also for additional reasons as mentioned above), we implanted CNTs with *silver* at a similar ion range, but the dose was increased 20-fold. HAADF images revealed an order of magnitude larger density of single atoms, few-atom clusters and also larger silver clusters, on the order of 1 nm in diameter. Random movements of atoms observed using both time- and through-focal-series, showed most silver atom constellations were attached to the surfaces with clusters being also formed within the CNTs. As an example, one frame of a BF/HAADF through-focus series is shown in Figs. 3(a) and 3(b). Interestingly, in addition to single atoms, bright chainlike and/or platelike features, whose movements are confined to the space between CNT walls and which represent one-dimensional and 2D intercalation aggregates, can be seen in HAADF images. Furthermore, it appears that 2D intercalation aggregates from neighboring interplanar spaces interact to form three-dimensional (3D) intercalation aggregates. Shown in Fig. 3(c) is the section in the light-framed area in Figs. 2(a) and 2(b) of selected images of the through-focus series. Running upward from the bottom left corner diagonally through the images, are the projections of the lattice planes (evident by the bright fringes) bordering vacuum on the left. The numbers above the images denote the defocus (in nm) of the e beam with respect to the CNT entrance surface, so from left to right the beam will be focused 8 nm below, 4 nm below, and 2 nm below, exactly on, 4 nm above and 8 nm above the entrance surface. The bright feature encircled with a light solid line comes into focus at -4 nm and goes out of focus at 0 nm. It represents an Ag-atom aggregate which is confined to the space between first and second outermost walls and can be seen to move slightly upward during repeated scans. The feature encircled with a dotted line represents a couple of Ag atoms; these come into focus at a different defocus value and hence must be incorporated at a different depth with respect to the beam-entrance surface compared to the atoms in the solid, light circle. The feature in the dashed, light circle is larger and can be seen at all defocus values, however, the

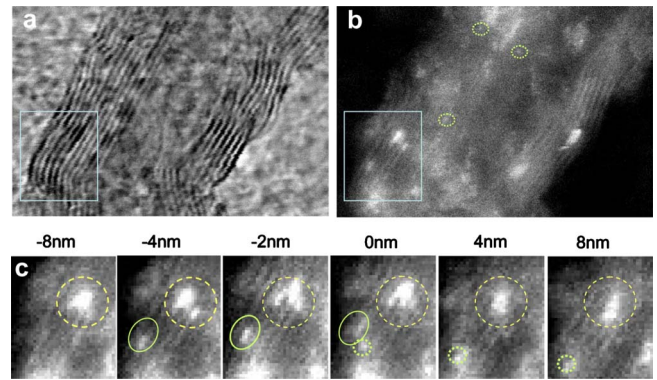


FIG. 3. (Color online) [(a) and (b)] SuperSTEM high-resolution BF and HAADF image of a multiple-walled CNT implanted with Ag at 200 eV and 2×10^{15} ions cm^{-2} . Like in Fig. 2(e) Ag-atom aggregates in the form of nanocrystals as well as single Ag atoms [some are encircled in (b)] are observed. (c) Selection of images from a through-focus HAADF image series, showing a part of the CNT wall projection in the frame in (a) and (b). Numbers above the images denote the defocus (in nm) of the e beam with respect to the CNT-entrance surface. The bright feature encircled with a solid line represents a planar Ag-atom aggregate confined to the space between two walls. The feature encircled with a dotted line represents a couple of intercalated Ag atoms. The feature in the dashed circle is a 3D aggregate consisting of several planar intercalation aggregates interacting across the CNT walls.

in-focus image appears to be near -2 nm. Close inspection reveals this feature to be a 3D aggregate consisting of several planar (very bright) intercalation aggregates separated by (darker) tube walls, i.e., the intercalants are situated between second and third, third and fourth, and fourth and fifth walls. The overall shape of the 3D aggregate changes in repeat scans as the planar aggregates move slightly relative to each other, however, they stay together as a cluster and seem to interact (be attracted) through the graphene sheets. In contrast, other whitish features, e.g., the cluster appearing as white area in the bottom left corner, move by crossing the CNT walls; in this case a silver nanocrystals have formed on the surface of the CNT. The described focus- and time-series analyses were performed on numerous CNTs, and it can be concluded that intercalation is achieved to a significant extent, albeit in a highly nonuniform fashion; effects of such intercalation on the band-structure properties will briefly be highlighted later.

Electronic dopants, *nitrogen* and *boron*, due to the similarity in atomic number with carbon, can unfortunately not be detected in HAADF images. However, their presence, and even local bonding environment, should be accessible in core-loss EELS. Nitrogen was implanted to a level giving on average one atom per square nanometer. A nitrogen-implanted multiwalled CNT is shown in the BF image in Fig. 4(a). Superposed is the raster defined for an SI with 1 nm^2 pixels. The spectra in the leftmost column [Fig. 4(c)] below represent raw data extracted from the bottom row of pixels indicated by the black arrow. They show the background-subtracted EEL intensity in the energy region around the nitrogen *K* edge. The tint of the pixel map in Fig. 4(a) represents the integrated intensity under the nitrogen *K*

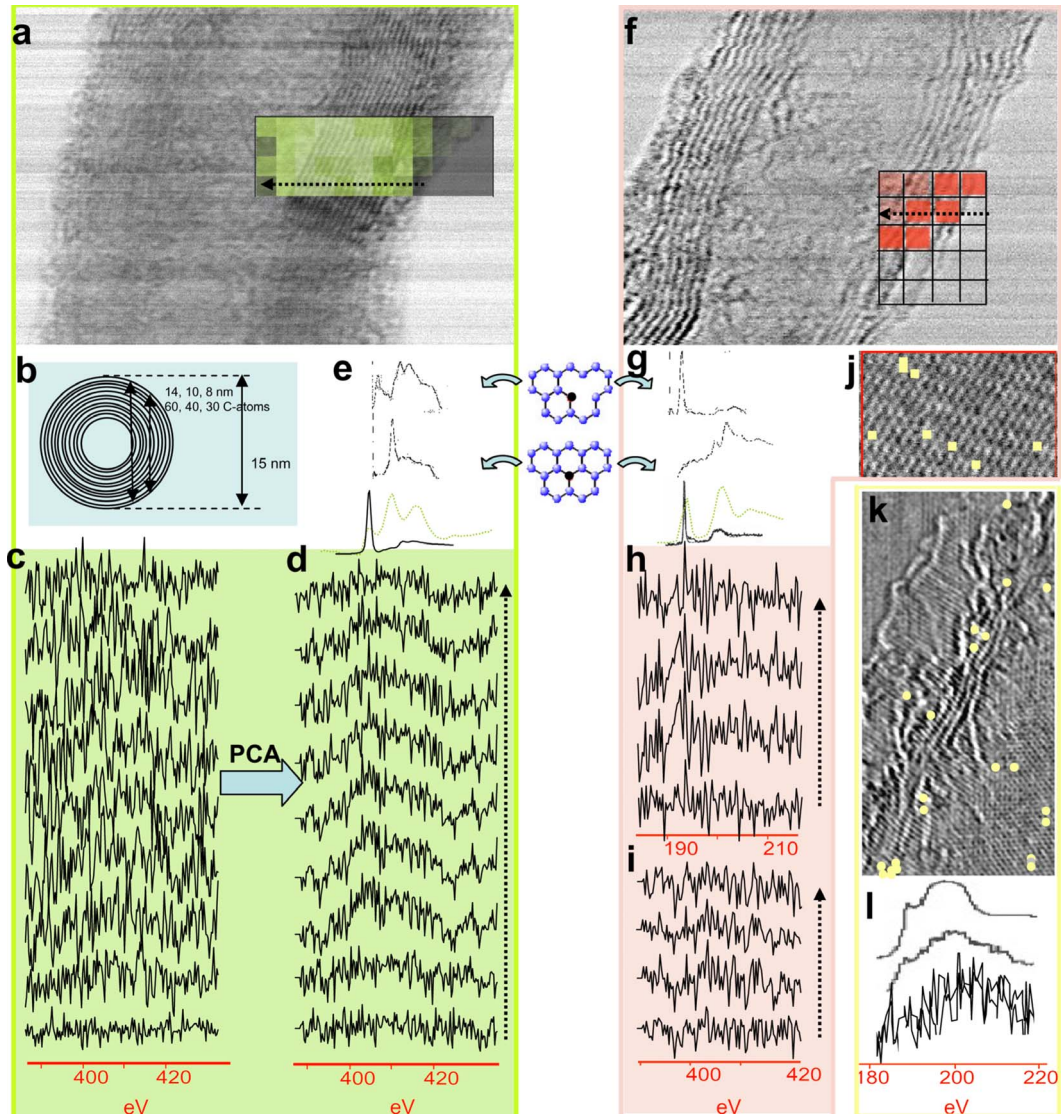


FIG. 4. (Color online) (a) SuperSTEM high-resolution BF image of a multiple-walled CNT ion implanted with nitrogen at 100 eV and 10^{14} ions cm^{-2} . The distance between the graphitic planes is 3.35 Å. Superimposed on the image is the EEL spectrum acquisition grid. Light gray (green) pixels indicate a captured nitrogen signal. The variation in tint of the pixels indicates the integrated intensity in the energy window 400–415 eV of the nitrogen signal of raw, background-subtracted spectra [like in (c) below]: a stronger intensity has a stronger (brighter) tint. (b) Approximate geometry and dimensions of the CNT in (a). (c) Raw EEL intensity in the energy region around the N K edge after power-law background subtraction, extracted from the bottom row of pixels in (a), indicated by the black arrow. (d) Same spectra after having undergone principal component analysis and normalization to the same noise bandwidth. (e) Top and middle spectra: DFT (WIEN2K) calculations of the N K EEL edge of substitutional N with and without adjacent vacancy in graphene, the structure model is shown in the middle of the figure with carbon atoms in gray (blue) and nitrogen atoms in black, bottom spectrum is of the N K edge in hexagonal BN (gray line; green) and nitrogen gas (black line). (f) SuperSTEM high-resolution BF image of a multiple-walled CNT implanted with boron at 100 eV and 10^{14} ions cm^{-2} . Superimposed on the image is the EEL spectrum acquisition grid. Dark gray (pink) pixels indicate captured boron signals. The variation in tint of the pixels indicates the integrated intensity of the boron signal in the energy window 190–193 eV: a stronger gray (pink) intensity has a stronger tint. (g) Top to bottom: DFT (WIEN2K) calculations of the B K EEL edge of substitutional B with and without adjacent vacancy in graphene, B K EEL edge of a hexagonal BN standard (Ref. 32) (gray; green) and of nonspatially resolved measurements of a highly boron doped (25%) multiple-walled CNT (black). (h) PCA treated, noise-normalized spectra extracted from the row of pixels in (f), indicated by the black arrow. (i) Signal in the energy region around the N K edge in the same spectra as in (h). (j) SuperSTEM high-resolution BF image of five-layered graphene with locations of π^* signals in the spectra, as in (h), at 190–193 eV, marked as white squares (yellow). (k) SuperSTEM high-resolution BF image of staggered graphene sheets; leftmost is a single layer, followed (toward the right) by a second sheet with a rough edge, which, in turn, is followed by four further graphene sheets with partially straight edges. B-signal positions are marked as white circles (yellow). (l) Top to bottom: B K EEL edge of amorphous B, of B_4C and of two typical, overlaid spectra from white (yellow) positions in (k). These signals are significantly above noise level, thus have not been PCA treated. The π^* peak is missing and comparison with the reference spectra suggests that small few-atom B clusters have formed attached to sheet edges or to monoatomic steps.

edge, and hence represents a visualization of the nitrogen-atom distribution (lighter gray–green online– tones correspond to higher intensity).

Although the EEL spectra and pixel map intensities seem to indicate a N *K* signal at ~ 400 eV, the statistical noise prevents meaningful interpretation. The rightmost column [Fig. 4(d)] shows the spectra, after principal-component analysis (PCA, e.g., Ref. 33) has been applied to the SI. This reduces the noise in the spectra significantly, and now the N *K*-edge signal can clearly be seen. The lowermost spectrum in both columns is from the edge of the tube-bordering vacuum, where no N signal can be detected. In spectra where no correlation of signal components exists with those of spectra in other pixels, in any given energy channel, the PCA enhances noise dramatically, hence all spectra were normalized to an identical noise “bandwidth.” Following PCA, the N *K*-edge signal of spectra from the CNT wall is adequately reconstructed so that fine structure is sufficiently revealed to enable comparison with reference or simulated spectra. The gray (green online) spectrum [Fig. 4(e)] above the right-hand column is a reference spectrum of boron nitride (BN) and the black spectrum of N₂. The two spectra above these are obtained from density-functional theory (DFT) calculations using the WIEN code³⁴ employing a substitutional N model and a model where substitutional N is paired with a vacancy. Through comparing DFT calculations with experimental EEL spectra, the captured inelastic signals can be characterized and general bonding configurations determined. Clearly, the experimental spectra give evidence of covalently bound N. Most of the spectra compare favorably with the substitutional N simulation and also with BN. Furthermore, nitrogen seems atomically dispersed in the graphene sheets without selectivity to specific structural features.

Shown in the sketch in Fig. 4(b) are approximate CNT dimensions and geometry. By comparing the signal integrals of nitrogen and carbon *K* edges [not shown in the spectra in Figs. 4(c) and 4(d)] over the same energy window, and taking into account the ratio of the inelastic scattering cross-sections for nitrogen and carbon ($\sigma_N/\sigma_C \approx \frac{1}{2}$) and the number, n_C , of carbon atoms in the atomic column encompassed by the beam, we obtain $n_N \approx 0.7(\pm 0.3)$ for the number of nitrogen atoms in the column. Since the beam is stepped in intervals of 1 nm, this yields a nitrogen concentration of slightly less than 1 atom per square nanometer and is in excellent agreement with the nominal implantation dose.

Boron was implanted at a low and a high dose. The low dose was the same as for nitrogen, namely, one atom per square nanometer. Figure 4(f) shows a BF image of a boron-implanted CNT with overlaid raster of pixel size 0.7 nm. This step size leads to slight oversampling, and from the tint of the pixels (darker corresponds to higher intensity in this case; pink coloration online) in the raster it can be seen that almost each pixel in the CNT contains a boron *K*-edge signal. Similar to the nitrogen dopants, boron dopants are disperse and uniform, and the detected signal density is in good agreement with the nominal dose. Figure 4(g) shows WIEN calculations of the boron *K* EEL edge for a boron-vacancy complex and for substitutional boron in graphene. Below these are experimental spectra of the boron *K* edge in BN and in multiple-walled CNTs doped to 25% with B.³⁵ Below

in Fig. 4(h) are PCA treated, noise-normalized spectra extracted from pixels of the SI in the raster in Fig. 4(f). The spectra are from the row marked with the arrow. The lowermost spectrum in Fig. 4(h) shows only noise; it corresponds to the rightmost pixel, where the e beam was not traversing the tube. The following two spectra (in ascending order) show a clear noise-reduced signal at 192 eV; we note that all gray-tinted (pink online) pixels in the raster in Fig. 4(f) show a clear signal at 192 eV, which very much resembles the π^* peak in the simulated spectrum of the boron-vacancy complex as well as that of the boron-doped tubes measured by Fuentes,³⁵ both shown in Fig. 4(g). The signal varies in strength: in the paler pixels the peak is weaker like in the uppermost spectrum in Fig. 4(h). The spectra in Fig. 4(i) from the same sequence of pixels as in Fig. 3(h) display a signal in the spectral region around the nitrogen *K* edge. The signal here is at noise level [compared to the nitrogen *K*-edge region in Fig. 4(d)], allowing one to deduce no significant number of nitrogen atoms exists.

Signals monitored in B-implanted few-layer planar graphene reveal the same distinct π^* peak as observed in the CNTs [two middle spectra in Fig. 4(h)] in positions highlighted by white squares (yellow online) in Fig. 4(j). Although it appears B is integrated substitutionally, the signal density is significantly lower, suggesting a lower (by almost an order of magnitude) B retention. Interestingly, the rather strong B signal obtained from staggered graphene sheets in Fig. 4(k) does not exhibit the π^* peak. Signal positions here coincide in most cases with the edge of graphene sheets: the leftmost portion of the image in Fig. 4(k) represents a single layer, followed (toward the right) by the “frayed” edge of a second sheet along which a number of signal positions are marked. This edge is followed by, to a large part, straight edges of four further graphene sheets, with a cluster of boron signal positions marked at the bottom left-hand corner of the image, and two further positions higher up along these edges. Two typical, overlaid spectra of the boron *K* edge are shown in Fig. 4(l); bottom. The signals were significantly above noise level and have not been PCA treated. Comparison with spectra of amorphous B [middle Fig. 4(l)] and B₄C [top Fig. 4(l)] suggests that small few-atom boron clusters have formed attached to sheet edges or monoatomic steps. It should be emphasized that these EEL results could not have been obtained had it not been for the 1 Å corrected probe: the image—as well as the EEL—signal would have been insignificant above the carbon background. The same applies to the HAADF results in the case of the metal implants.

Pomoell *et al.*³⁶ estimated that ions ranging from carbon to xenon loose on average 300 eV when penetrating a single-walled CNT, i.e., 150 eV per graphene sheet. According to this, double-walled CNTs should stop all ions we have implanted. The majority of our CNTs had more than two walls and all ions should have been stopped; hence the low Co retention is surprising. The number of silver, boron, and nitrogen atoms can be accounted for; silver forms intercalants and nanocrystalline agglomerates, whereas boron and nitrogen appear to be homogeneously incorporated into the nanotube graphene sheets. In contrast, the boron retention in free-standing planar few-layered graphene is very low; in the case of staggered sheets it appears that boron atoms have not been

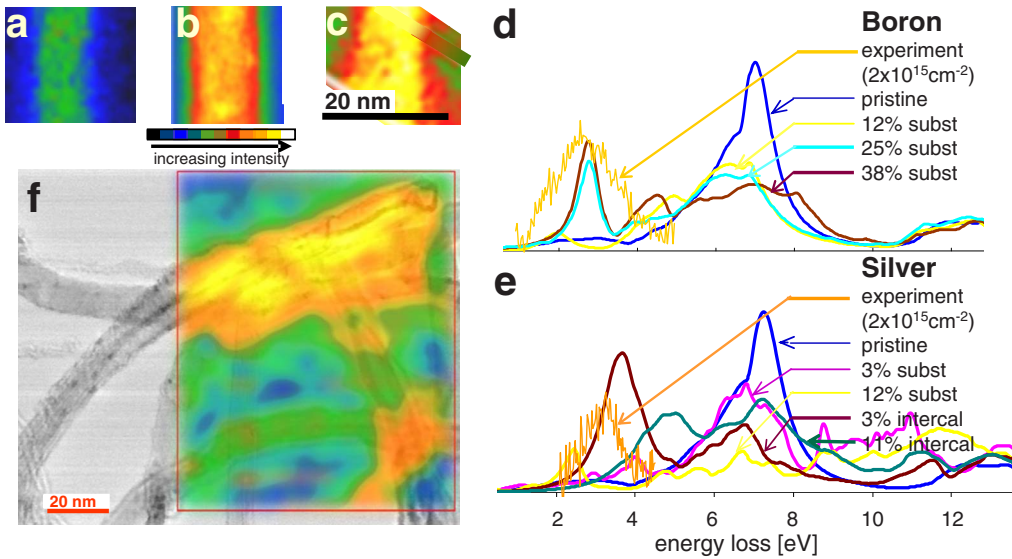


FIG. 5. (Color online) (a) EEL intensity distribution extracted from SIs at 2.6–3.4 eV in a pristine, (b) a Ag-implanted and (c) a B-implanted nanotube (both implanted at 200 eV and $2 \times 10^{15} \text{ ions cm}^{-2}$) with intensities displayed on the same scale. The implantation has created a plasmon at uv/visible energies, as predicted by the DFT EEL-spectra calculations, using WIEN2K, of (d) substitutional B and (e) substitutional and intercalated Ag in layered carbons. Experimental spectra are overlaid. (f) Plasmon-intensity distribution overlaid on a BF-NorthWestSTEM image of a B-implanted CNT network [intensity displayed on a reduced scale compared to (c)], showing “hot spots,” where tubes are in close proximity.

incorporated at all but aggregate at surface steps. These findings could arise from two possible scenarios: (i) the ions have not been sufficiently stopped and traversed few graphene sheets; reasonable numbers of implants were only monitored in locations of CNTs projections where the traversed thickness was maximal. (ii) The ions have not possessed sufficient energy to penetrate even one layer of graphene, and the reason that indeed a large retention was monitored in the CNTs in locations of vertical-wall projections is that here the ions could channel between the graphene sheets. Both scenarios would explain pixel-intensity maps in Figs. 4(a) and 4(f), i.e., the implanted-ion density is greatest where sheets have near-vertical [scenario (i)] or vertical [scenario (ii)] projections and reduces considerably toward the center of the CNTs, where the implanted ions impinge perpendicularly onto the sheets. The latter scenario, however, additionally accounts for observation of many ions on surfaces [in particular, for the graphene sample in Fig. 4(k)].

In the same paper Pomoell *et al.* further derived that at an implantation energy of 100 eV, the number of coordination defects (damage) per incident ion with Z spanning carbon to xenon, ranges from 3.5–5.5; for 200 eV implants this number increases to 7–10. As mentioned above we compared high resolution electron microscopy (HREM) images of unimplanted pristine nanotubes with those of implanted ones (Fig. 1), and did not observe significant changes in the overall microstructure. The tubes utilized in all cases herein were from the same sample and had a portion of crumpled tubes alongside straight ones, and this portion did not change noticeably after implantation. Thus, on the basis of HREM images, we do not observe damaging due to implantation.

Brzhezinskaya *et al.*³⁷ taken the downward shift in energy of the π plasmon as measure of the damage introduced dur-

ing Ar ion implantation. We believe this is not a good indicator (i) because the π -plasmon band structure will be modified by functional and metal dopants and (ii) there is, in any case, an energy dependence of the π plasmon on the e-beam direction and distance from the nanotube surface, which, in the case of small diameter tubes, is difficult to separate from implantation effects. Analysis of the peak energies of the bulk plasmon in pristine and implanted nanotubes of similar sizes showed that they are very similar, although slight changes in the overall shape of the plasmon could be detected, with the implanted samples exhibiting structure in the low-energy tail (to be published). However, we ascribe this to modification of the plasmon band structure by the dopants, rather than to damage.

Finally, in Fig. 5 we show first results of modification of the electronic band structure of CNTs by ion implantation. Calculations predict creation of an intense plasmon at 2.5 eV in CNTs with substitutional boron at the high doping level of $\sim 30\%$ [Fig. 5(d), turquoise and purple curves online] and at 3.7 eV for intercalated silver at $\sim 3\%$ doping [Fig. 5(e), purple curve online]. Experimental spectra for boron- and silver-implanted CNTs at $2 \times 10^{15} \text{ cm}^{-2}$ are superposed on the simulated EEL spectra. When implanted and retained in a single graphene sheets, this dose would be equivalent to $\sim 30\%$ doping. In the case of boron implanted in CNTs [see results of Figs. 4(f) and 4(h)] we have an indication of good retention, and although not all the boron is retained in a single-carbon sheet the existence of the plasmon at ~ 2.5 eV [Fig. 5(d) experimental curve; orange online] is therefore to be expected, and corroborated by the calculations for $>25\%$ substitutional boron. Furthermore, from the above results, the retention of silver in intercalated form was by far lower (silver mostly formed nanocrystals on the outside of the CNT). It is therefore feasible that the experiment here shows

a plasmon due to less than 3% intercalated silver, thus accounting for the redshift of the plasmon peak in comparison to the calculation for 3% intercalated silver. The experimental spectra in Figs. 5(d) and 5(e) are extracted from SIs. Figures 5(a)–5(c) show intensity maps of energy losses at ~ 2.6 – 3.4 eV in individual nanotubes, obtained after removal of the zero-loss peak and diffraction-contrast effects from the spectra. The plasmon-intensity maps, although not calibrated for absolute intensities, are on the same scale: according to this a silver-implanted CNT [Fig. 5(b)] reveals twice and a boron-implanted CNT [Fig. 5(c)] four times the intensity of a pristine tube [Fig. 5(a)] at optical energies (intensities are displayed on a temperature scale online). Pristine CNTs have no plasmons of significant intensity at energies below the 6 eV π plasmon.

The resonances in the implanted tubes are complex with submodes below 3 eV and enhancement of the native CNT π plasmon. Hence further investigations, concerning plasmon coupling, hybridization, intensity, radiative/nonradiative nature, are highly desirable. However, our findings so far are in line with previous investigations: intercalation with alkali, transition, or noble metals has been reported to introduce “Drude” plasmons in graphite.²² Boron has been found to introduce valence absorption, suggested to be the predecessor of the strong “intragap” plasmon, also observed in acceptor intercalation compounds when more charge is depleted from the graphite planes.³⁸ Other elements might bear even greater potential, if they could be introduced “cleanly” into the nanotube walls by controlled doping.

In this contribution we have demonstrated that introduction of dopant atoms into nano-objects through the use of ion implantation, where dose and spatial density of the dopant can be controlled, is possible, although further investigation into implantation-energy and -dose dependence would be required to clarify the retention issue. In principle, variation in the implantation energy should enable surface deposition through to depth implantation to be accomplished. A most exciting aspect is the controlled introduction of damage simultaneously with the doping, to “roughen” the CNT surfaces: this could serve to transform nonradiative into radiative plasmons to enable coupling with light, which would open up a plethora of new applications for CNTs in light emission, guiding and harvesting. The development, fabrication, and functionalization of these materials are becoming increasingly dependent on atomic-scale characterization enabling measurement of the bonding state of individual dopant atoms in location. Through careful optimization of acquisition conditions in a high-performance, aberration-corrected STEM this has now become a reality.

ACKNOWLEDGMENTS

We gratefully acknowledge A. Scott of the University of Leeds for his kind help and instruction in using the WIEN2K code, J. Eccles for assistance with PCA analysis, R. R. Nair for graphene membrane supply (all from the University of Manchester), and M. Reading (from the University of Salford) for carrying out with the ion implantations.

APPENDIX: AUXILIARY MATERIAL

1. Specimen preparation

The common method of chemical doping invariably results in involuntary codoping, which changes the microstructural site and coordination of the intended dopant significantly, and almost always provides contaminated substrates.³⁹ Ultralow-energy ion implantation^{40,41} introduces hardly any damage has been suggested as conceivably representing the purest doping method available and constitutes a method well suited for mass semiconductor production. Ion implantation can also be site selective through use of a macroscopic mask. Ion implantation was carried out into TEM-ready samples: CNTs were dispersed by sonication in distilled water with the solution dripped onto carbon-coated TEM copper-mesh grids. Graphene samples were obtained using micromechanical cleaving and exfoliation from HOP graphite (explained in detail in Ref. 29). Following low-energy ion implantation of CNTs, B- and N-dopant atoms appear to be uniformly dispersed and have not formed chemical or structural phases, in stark contrast to observations for chemically doped CNTs. Silver atoms form nanoclusters or intercalate.

2. Signal capture and radiation damage

Obtaining the best possible signal-to-noise ratio while avoiding beam damage represents a long-standing problem in microscopy. The theoretical value for knock-on damage is 120 keV, although a value of ~ 100 keV is consistent with our observations of damage. Close comparison of microstructure both pre- and post-EELS acquisitions, confirmed radiation effects could be neglected in the selected data. Some data (of the silver implants) were obtained with a reduced voltage of 80 keV. Conditions for core-loss data acquisition were a trade-off between reasonable statistics, beam damage, drift, and raster size (as 1 spectrum per square nanometer had to be obtained to avoid undersampling). An acquisition time of 1 s per pixel was proven to give optimal results. The signal in the low-loss spectra was orders of magnitude stronger, and in order to retain the inherent energy resolution of the tip (≤ 0.3 eV) and to counter deterioration of monochromation arising from voltage instabilities the spectrum image area was oversampled at very short acquisition times per pixel (< 0.1 s per pixel), the zero-loss peaks in each spectrum then realigned and the spectrum images rebinned.

3. Data analysis

Immediately following raw SI acquisition, dark current consisting of thermal excitations in the charge coupled device detector was acquired. Avoiding dark current collection during SI acquisition decreased the total collection time of an EEL data set. Following subtraction of dark current from the raw SI, energy drift was corrected. In contrast to dopant signals, the carbon signal does not arise from one single atom, but rather from several tens of carbon atoms in a graphitic environment. Core-loss spectra were thus calibrated with re-

spect to the carbon π^* -peak maximum and low-loss spectra with respect to the zero-loss peak. Within a spectrum image, all spectra were identically background-fitted and consequently background-subtracted using a power-law function. The number of atoms giving rise to a signal was deduced from the jump ratio and the relative scattering cross-sections of absorption edges with respect to the carbon edge, with all edge intensities integrated over windows of ~ 20 eV from their onset. The number of carbon atoms was estimated from the dimensions of the sample obtained from HREM BF images.

4. DFT simulations

Hohenberg and Kohn⁴² showed the Schrödinger equation, formulated as an equation of an N-electron wave function of

3N variables, could be expressed as an equation of the electron density with only three variables, leading to the formation of the DFT method. DFT calculations demonstrated have had much success in explaining the electron loss near edge structure (ELNES) of graphitic systems, accurately representing the weak-energy dependence of transition-matrix elements.⁴³ Present DFT calculations were performed utilizing the *ab initio* full potential linearized augmented plane-wave computer program WIEN2K.³⁴ The muffin-tin radii were set at $R=1.34$ a.u. for both carbon and dopant atoms. 250 k points were utilized, as representative of infinite sampling of the Brillouin zone of graphite. Self-consistent iterations were performed until convergence (0.1 eV) on the total energy. An Rk max value of 7 was used; this product indicates the accuracy of the basis set used, where k max represents the maximum k value in the expansion of plane waves.

*ursel.bangert@manchester.ac.uk

- ¹P. M. Voyles, D. A. Muller, J. L. Grazul, P. H. Citrin, and H. J. L. Gossman, *Nature (London)* **416**, 826 (2002).
- ²J. A. Misewich, R. Martel, Ph. Avouris, J. C. Tsang, S. Heinze, and J. Tersoff, *Science* **300**, 783 (2003).
- ³F. Schedin, A. K. Geim, S. V. Morozov, E. W. Hill, P. Blake, M. I. Katsnelson, and K. S. Novoselov, *Nature Mater.* **6**, 652 (2007).
- ⁴C. W. Zhou, J. Kong, E. Yenilmez, and H. J. Dai, *Science* **290**, 1552 (2000).
- ⁵S. Maldonado and S. Morin, *Carbon* **44**, 1429 (2006).
- ⁶S. M. C. Vieira, O. Stéphan, and D. L. Carroll, *J. Mater. Res.* **21**, 3058 (2006).
- ⁷W.-H. Zhang and W.-D. Zhang, *Sens. Actuators B* **134**, 403 (2008).
- ⁸T. Takenobu, T. Takano, M. Shiraishi, Y. Murakami, M. Ata, H. Kataura, Y. Achiba, and Y. Iwasa, *Nature Mater.* **2**, 683 (2003).
- ⁹W. Feng, K. Kamide, F. Zhou, H. Araki, X. G. Wang, and K. Yoshino, *Jpn. J. Appl. Phys., Part 2* **43**, L36 (2004).
- ¹⁰J. E. Fischer, *Acc. Chem. Res.* **35**, 1079 (2002).
- ¹¹J. W. Jang, C. E. Lee, S. C. Lyu, T. J. Lee, and C. J. Lee, *Appl. Phys. Lett.* **84**, 2877 (2004).
- ¹²R. Z. Ma, D. Golberg, Y. Bando, and T. Sasaki, *Phil. Trans. Roy. Soc.* **362**, 2161 (2004).
- ¹³D. Golberg, Y. Bando, L. Bourgeois, K. Kurashima, and T. Sato, *Carbon* **38**, 2017 (2000).
- ¹⁴P. L. Gai, O. Stéphan, K. McGuire, A. M. Rao, M. S. Dresselhaus, G. Dresselhaus, and C. Colliex, *J. Mater. Chem.* **14**, 669 (2004).
- ¹⁵M. Terrones, P. Redlich, N. Grobert, S. Trasobares, W. K. Hsu, H. Terrones, Y. Q. Zhu, J. P. Hare, C. L. Reeves, A. K. Cheetham, M. Ruhle, H. W. Kroto, and D. R. M. Walton, *Adv. Mater.* **11**, 655 (1999).
- ¹⁶L. Duclaux, *Carbon* **40**, 1751 (2002).
- ¹⁷G. Sumanasekera, J. Allen, and P. Eklund, *Mol. Cryst. Liq. Cryst.* **340**, 535 (2000).
- ¹⁸A. S. Claye, N. M. Nemes, A. Janossy, and J. E. Fischer, *Phys. Rev. B* **62**, R4845 (2000).

- ¹⁹R. S. Lee, H. J. Kim, J. E. Fischer, A. Thess, and R. E. Smalley, *Nature (London)* **388**, 255 (1997).
- ²⁰A. S. Claye, J. E. Fischer, C. B. Huffman, A. G. Rinzier, and R. E. Smalley, *J. Electrochem. Soc.* **147**, 2845 (2000).
- ²¹T. Miyake and S. Saito, *Phys. Rev. B* **65**, 165419 (2002).
- ²²X. Liu, T. Pichler, M. Knupfer, and J. Fink, *Phys. Rev. B* **67**, 125403 (2003).
- ²³H. Raether, *Physics of Thin Films* **9**, 145 (1997).
- ²⁴R. de Waele, A. F. Koenderink, and A. Polman, *Nano Lett.* **7**, 2004 (2007).
- ²⁵P. Trouillas, A. Moliton, and B. Ratier, *Synth. Met.* **73**, 145 (1995).
- ²⁶A. Kumar, P. Thakur, N. B. Brookes, and D. K. Avasthi, *Appl. Phys. Lett.* **95**, 182511 (2009).
- ²⁷A. V. Krashennnikov and F. Banhart, *Nature Mater.* **6**, 723 (2007).
- ²⁸N. Grobert, M. Terrones, S. Trasobares, K. Kordatos, H. Terrones, J. Olivares, J. P. Zhang, P. Redlich, W. K. Hsu, C. L. Reeves, D. J. Wallis, Y. Q. Zhu, J. P. Hare, A. J. Pidduck, H. W. Kroto, and D. R. M. Walton, *Appl. Phys. A: Mater. Sci. Process.* **70**, 175 (2000).
- ²⁹T. J. Booth, P. Blake, R. R. Nair, D. Jiang, E. W. Hill, U. Bangert, A. Bleloch, M. Gass, K. S. Novoselov, M. I. Katsnelson, and A. K. Geim, *Nano Lett.* **8**, 2442 (2008).
- ³⁰P. Goodhew and A. Bleloch, *Mater. World* **11**, 23 (2003).
- ³¹J. A. Hunt and D. B. Williams, *Ultramicroscopy* **38**, 47 (1991).
- ³²J. Nelayah, M. Kociak, O. Stéphan, F. J. G. de Abajo, M. Tence, L. Henrard, D. Taverna, I. Pastoriza-Santos, L. M. Liz-Marzan, and C. Colliex, *Nat. Phys.* **3**, 348 (2007).
- ³³N. Borglund, P. G. Astrand, and S. Csillag, *Microsc. Microanal.* **11**, 88 (2005).
- ³⁴M. Nelhiebel, P. H. Louf, P. Schattschneider, P. Blaha, K. Schwarz, and B. Jouffrey, *Phys. Rev. B* **59**, 12807 (1999).
- ³⁵G. G. Fuentes, E. Borowiak-Palen, T. Pichler, X. Liu, A. Graff, G. Behr, R. J. Kalenczuk, M. Knupfer, and J. Fink, *Phys. Rev. B* **67**, 035429 (2003).
- ³⁶J. Pomoell, A. V. Krashennnikov, K. Nordlund, and J. Keinonen, *Nucl. Instrum. Methods B* **206**, 18 (2003).
- ³⁷M. M. Brzhezinskaya, E. M. Baitingera, and V. V. Shnitov,

- [Physica B **348**, 95 \(2004\).](#)
- ³⁸H. Pan, Y. P. Feng, and J. Y. Lin, [Phys. Rev. B **73**, 035420 \(2006\).](#)
- ³⁹N. Grobert, [Mater. Today **10**, 28 \(2007\).](#)
- ⁴⁰T. Kamimura, K. Yamamoto, T. Kawai, and K. Matsumoto, [Jpn. J. Appl. Phys., Part 1 **44**, 8237 \(2005\).](#)
- ⁴¹K. Yamamoto, T. Kamimura, and K. Matsumoto, [Jpn. J. Appl. Phys., Part 1 **44**, 1611 \(2005\).](#)
- ⁴²P. Hohenberg and W. Kohn, [Phys. Rev. **136**, B864 \(1964\).](#)
- ⁴³J. T. Titantah and D. Lamoen, [Phys. Rev. B **72**, 193104 \(2005\).](#)